Energy-overlap of the Dirac surface state with bulk bands in $SnBi_2Te_4$

S. V. Eremeev,[1] O. De Luca,[2,3] P. M. Sheverdyaeva,[4] L. Ferrari,[5] A. V. Matetskiy,[4] G. Di Santo,[6] L. Petaccia,[6] C. Crovara,[2] T. Caruso,[2,3] M. Papagno,[2,3] R. G. Agostino,[2,3] Z. S. Aliev,[7] P. Moras,[4] C. Carbone,[4] E. V. Chulkov,[8,9,10,11] and D. Pacilè[2,*]

[1]Institute of Strength Physics and Materials Science, 634055 Tomsk, Russia
[2]Dipartimento di Fisica, Università della Calabria (Unical), 87036 Rende (CS), Italy
[3]STAR Research Infrastructure, Università della Calabria, Via Tito Flavio, 87036 Rende (CS), Italy
[4]Istituto di Struttura della Materia-CNR (ISM-CNR), 34149 Trieste, Italy
[5]Istituto di Struttura della Materia, Consiglio Nazionale delle Ricerche, 00133 Roma, Italy
[6]Elettra Sincrotrone Trieste, 34149 Trieste, Italy
[7]Baku State University, AZ1148 Baku, Azerbaijan
[8]Departamento de Polímeros y Materiales Avanzados: Física, Química, y Tecnología, Facultad de Ciencias Químicas, Universidad del País Vasco UPV/EHU, 20080 San Sebastián/Donostia, Spain
[9]Donostia International Physics Center (DIPC), 20018 Donostia-San Sebastián, Basque Country, Spain
[10]Centro de Física de Materiales (CFM-MPC), Centro Mixto CSIC-UPV/EHU, 20018 Donostia-San Sebastián, Basque Country, Spain
[11]Saint Petersburg State University, 199034 Saint Petersburg, Russia

(Received 20 October 2022; accepted 5 January 2023; published 23 January 2023)

Topological insulators in which the Fermi level is in the bulk gap and intersects only a topological surface state (the Dirac cone) are of special interest in the current research. In the last decades, a fine-tuning of the chemical composition of topological insulators has been carefully explored in order to control the Fermi level position with respect to the Dirac surface state. Taking the $SnBi_2Te_4$ crystal as a case study, we provide a characterization of its electronic structure by means of angle-resolved photoemission spectroscopy and first-principles calculations. We show that, going away from the Brillouin zone center, bulk band states energetically overlap with the Dirac cone at the Fermi level, thus providing an unwanted as well as hidden contribution to the transport properties of the material. In addition, the comparison between experimental results of the band structure with state-of-the-art simulations, implemented taking into account the number of defects, leads to useful insights on the existing limits in the description of this material.

DOI: 10.1103/PhysRevMaterials.7.014203

I. INTRODUCTION

Spintronic devices based on topological insulators (TIs) are known to provide very efficient spin-to-charge conversion [1–6], owing to the presence of topologically protected surface states (TSSs), which exhibit a Dirac-like dispersion behavior coupled to a spin-momentum locking. The energy of the Dirac point, where the branches of the TSS cross, and its overlap with the bulk bands at the Fermi level (E_F) determine the topological or trivial transport behavior of the material. In order to fully exploit the transport properties of TSSs in spintronic devices, contributions from the bulk conduction band (BCB) in proximity of E_F need to be removed. Starting from pioneering works [7–9], the engineering of the bulk stoichiometry through hole and electron doping was shown as a successful route to modify the electronic and spin properties of bismuth-based binary chalcogenides. Among several approaches, recent studies [10,11] confirmed that by tuning the Bi/Sn ratio in favor of the Sn content it is possible to shift the TSS into the bulk band gap. For example, such a design of TIs was demonstrated to maximize the spin-to-charge conversion involving TSSs and to allow for THz emission when the TI film is combined to ferromagnetic materials [10]. More specifically, in Ref. [11] the coexistence of the BCB and the TSS at E_F was carefully explored and related to the amount of Sn for different films of TIs grown on InAs(111)/Si(111) substrates (Bi_2Te_3, $SnBi_4Te_7$, $SnBi_2Te_4$, and $Sn_{1-x}Bi_xTe$). These results showed that, for selected film thicknesses, the contribution of the BCB at the center of the surface Brillouin zone (SBZ) is minimum for $SnBi_2Te_4$. On the other hand, on nanoplates of $SnBi_2Te_4$, a previous study [12] reported longitudinal magnetotransport measurements showing a weak antilocalization effect at low temperature, which was attributed to a residual bulk contribution across E_F. The existing literature on the experimental band structure of bismuth-based ternary chalcogenides, such as $GeBi_2Te_4$ [13], $PbBi_2Te_4$ [14], and $SnBi_2Te_4$ [11], mainly reports on the overlap of TSSs with the BCB at the BZ center, where indeed TSSs are detected, although other overlapping regions along the $\bar{\Gamma}$-$\bar{M}$ direction of the SBZ were reported [15–17].

In this paper, we investigate the potential of substituting Sn atoms in bismuth-based binary chalcogenides [10,11] using $SnBi_2Te_4$ as a case study. By means of angle-resolved

*daniela.pacile@fis.unical.it

 ©2023 American Physical Society

photoemission spectroscopy (ARPES) and first-principles calculations we identify the energy-momentum space location of bulk continuum states that energetically overlap with the TSS in the proximity of E_F, thus affecting the topological transport behavior of the material. In addition, the in-plane lattice parameter of $SnBi_2Te_4$ is very close to that in $MnBi_2Te_4$ (4.33 Å), the intensively investigated antiferromagnetic TI (AFM-TI) [18]. Therefore, $SnBi_2Te_4$ is highly attractive for designing lattice-matched van der Waals (vdW) heterostructures composed of nonmagnetic and magnetic structural blocks. We show that in $SnBi_2Te_4$, besides a residual BCB at the $\bar{\Gamma}$ point, a contribution of the BCB crossing E_F is present in the energy-momentum space along the $\bar{\Gamma}$-$\bar{M}$ direction of the SBZ, along which also the bulk valence band (BVB) energetically overlaps with the TSS. Furthermore, we show density functional theory (DFT) simulations obtained by including the Bi/Sn antisite defects, which are known to significantly influence the overall electrical properties of TIs [19,20]. We find a partial agreement with the experimental results and discuss existing limits in state-of-the-art simulations to describe the electronic structure of TIs.

The present case study system provides useful insights on the band structure of TIs with the focus on the hidden energy overlap of TSSs with bulk states.

II. METHODS

Single-crystalline ingots of $SnBi_2Te_4$ were grown from nonstoichiometric composition by the vertical Bridgman-Stockbarger method [21]. The synthesis was performed in two steps. First, the polycrystalline composition was synthesized from high-purity (5N) elements in an evacuated quartz ampule at about 1000 K for 8 h mixing incessantly, followed by air cooling. Afterward, the polycrystalline sample was placed in a conical-bottom quartz ampule, which was sealed under a vacuum better than 10^{-4} Pa. At the beginning of the growing process, the ampule was held in the “hot” zone (≈920 K) of a two-zone tube furnace for 24 h for a complete melting of the composition. The charged ampule moves from the “hot” zone to the “cold” zone with the required rate 1.0 mm/h. In this way, the bulk ingot with average dimensions of ≈4 cm in length and 0.8 cm in diameter was obtained. The single-crystal structure of the as-grown $SnBi_2Te_4$ ingot was verified by accurate x-ray diffraction measurements (see Fig. S1 of the Supplemental Material [22]).

The photoemission measurements were performed on surfaces obtained by cleavage at room temperature (RT) in ultrahigh-vacuum (UHV) conditions. The cleaved surfaces were stable for several days in UHV. The high-quality single-crystalline (0001) surface was verified by the sharp features in the low energy electron diffraction (LEED) pattern (see inset of Fig. S2(a) of the Supplemental Material [22]). The chemical compositions of TI samples have been checked by core level measurements, reported in Fig. S2 of the Supplemental Material [22], where the sharpness of selected photoemission peaks and the absence of contaminants, like oxygen, demonstrate the high quality of samples. Low-energy ARPES measurements (16 eV and 20 eV beam energy) were carried out at the BaDElPh beamline [23] of the Elettra synchrotron light laboratory at 80 K, with energy resolution of about 20 meV, and momentum resolution of ∼0.02 $Å^{-1}$. Higher-energy ARPES measurements were carried out at the VUV-Photoemission beamline of Elettra at 9 K, with energy resolution of about 20 meV and angular resolution better than 0.3°.

Scanning tunneling microscopy (STM) measurements were performed at Unical in UHV conditions with an Aarhus SPM 150 equipped with KolibriSensor from SPECS, operated via Nanonis control system. STM images were acquired at RT in constant-current mode with a W tip cleaned in UHV by repeated cycles of Ar^+ sputtering. Tunneling current and voltage are labeled with I_t and V_b, respectively. All STM images were processed using the WSxM software [24].

The electronic structure calculations were carried out using the projector augmented wave method (PAW) [25] implemented in the VASP package [26–28]. The exchange-correlation effects were taken into account using Perdew-Burke-Ernzerhof generalized gradient approximation (GGA-PBE) [29]. Spin-orbit coupling was treated using the second variation method [30]. The DFT-D3 method [31] was used to accurately describe the van der Waals interaction. In addition to GGA-PBE used in earlier calculations we adopted the semilocal modified Becke-Johnson (mBJ) exchange potential [32,33] for $SnBi_2Te_4$ bulk. For surface band structure calculations we use the slab model and apply the Slater-type DFT-1/2 self-energy correction method [34,35] with a partially (quaternary) ionized tellurium potential as an alternative to the mBJ approach which diverges for surface calculations. Before using the DFT-1/2 method for surface calculation we compared its results for the bulk with mBJ spectra. To treat the Sn-Bi intermixing we employed a virtual crystal approximation (VCA) as implemented in the ABINIT code [36], where the averaged potential of a virtual atom occupying a site in the Sn/Bi sublattice is defined as a mixture $V_{VCA} = xV_{Sn} + (1 - x)V_{Bi}$ of Sn (V_{Sn}) and Bi (V_{Bi}) pseudopotentials. In ABINIT calculations we used GGA-PBE Hartwigsen-Goedecker-Hutter (HGH) relativistic norm-conserving pseudopotentials which include the spin-orbit interaction [37]. All slab calculations were carried out within the repeating slabs of six septuple layers thickness with vacuum layer thickness of ∼10 Å.

III. RESULTS AND DISCUSSION

The $SnBi_2Te_4$ TI crystallizes in a trigonal structure with hexagonal unit cell, where septuple-layer (SL) blocks [Te-Bi-Te-Sn-Te-Bi-Te] are stacked along the c axis, as shown in Fig. S1 of the Supplemental Material [22]. The bonds inside the SL have mainly ionic-covalent character, whereas the blocks are held together by weak van der Waals forces [38]. The structural properties of TI samples have been investigated by LEED [22] and STM. In Fig. 1(a) we show, on a large scale, the cleaved surface of $SnBi_2Te_4$, which exhibits atomically flat terraces several hundreds of nm in size, with a step height of 13.9(2) Å, as extracted from line profiles shown representatively in Fig. 1(b). This value is in agreement with the thickness of a single $SnBi_2Te_4$ SL, which is equal to one-third of the vertical bulk parameter [$c = 41.490(7)$ Å], as found from x-ray diffraction (Fig. S1 of the Supplemental Material [22]). Figure 1(c) shows an atomically resolved STM image

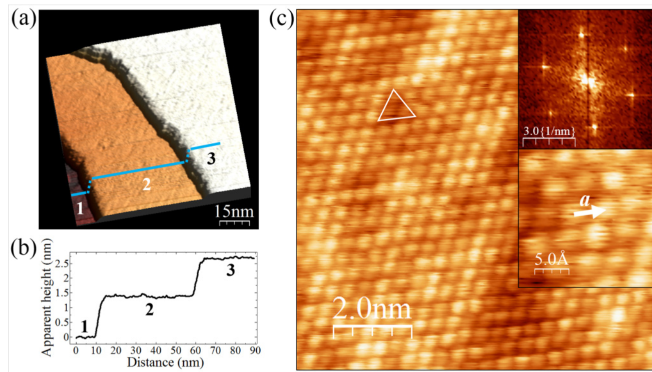

FIG. 1. (a) Constant-current STM image on fresh cleaved $SnBi_2Te_4$ ($V_b = 2$ V; $I_t = 100$ pA; $T = 300$ K). (b) Apparent height profile along the blue line in (a) revealing the presence of terraces with similar step height, corresponding to the SL atomic block. (c) Atomically resolved STM image of the surface ($V_b = 310$ mV; $I_t = 400$ pA; $T = 300$ K). The upper inset shows the Fourier transforms of panel (c). The lower inset shows a zoom of 4 nm^2.

of $SnBi_2Te_4$ exhibiting hexagonal periodicity, also seen by the Fourier analysis reported in the upper inset. Atomic-resolved STM images provide a planar lattice constant of 4.3(2) Å, shown in the lower inset of Fig. 1(c), in agreement with x-ray diffraction data (Fig. S1 of the Supplemental Material [22]). A deeper inspection revealed dark triangular-like defects [highlighted by a white triangle in Fig. 1(c)] with an average density of about 6% at the surface, i.e., in the upper atomic layers of the SL block. These defects are the result of a different local density of states (LDOS) at the surface, as found in several other TIs [19,20,39]. They have been ascribed to substitution of the Bi atoms in the subsurface layer of the SL block by the Sn atoms of the central layer.

In Fig. 2 we report ARPES data measured along $\bar{\Gamma}$-$\bar{M}$ of the surface Brillouin zone (SBZ) [Fig. 2(a)], in the following k_x, using different photon energies. Photoemission measurements taken at 70 eV [Fig. 2(b)] allow us to investigate the first and second SBZ of the energy-momentum space. These data provide clear evidence of a TSS in the energy region between 0.40 eV and E_F, i.e., Dirac cone branches intersecting at the SBZ center. We also observe M-shaped BVB with an energy maximum slightly above the Dirac point, at about 0.30 eV binding energy, and $k_x = \pm 0.15$ Å^{-1} at the selected photon energy. These data are in a good agreement with previous observations [10,11], besides an energy shift. Other bulk valence bands approaching E_F cannot be seen under these experimental conditions.

In Figs. 2(c) and 2(d) we show ARPES data taken at 20 eV and 16 eV photon energy, respectively. First, we notice in Fig. 2(c), beside the TSS centered at the $\bar{\Gamma}$ point, a strong intensity near E_F due to the BCB and the Rashba states, which have been observed in other TIs with vdW-layered atomic structure [15,40–45]. These states have been ascribed to an expansion of van der Waals gaps during the growth process, induced by imperfections/defects trapped between neighboring blocks [41,46,47]. From Fig. 2(c), we estimated the Dirac point position to be at 0.36 eV binding energy, and carefully checked its stability after 1 minute of beam exposure up to several hours. However, we cannot rule out that, within the first seconds of beam exposure required to perform an ARPES measurement, the Dirac point shifts downward by tens of meV due to band bending, as estimated in a dedicated study on a broad family of TIs [48]. The group velocity of

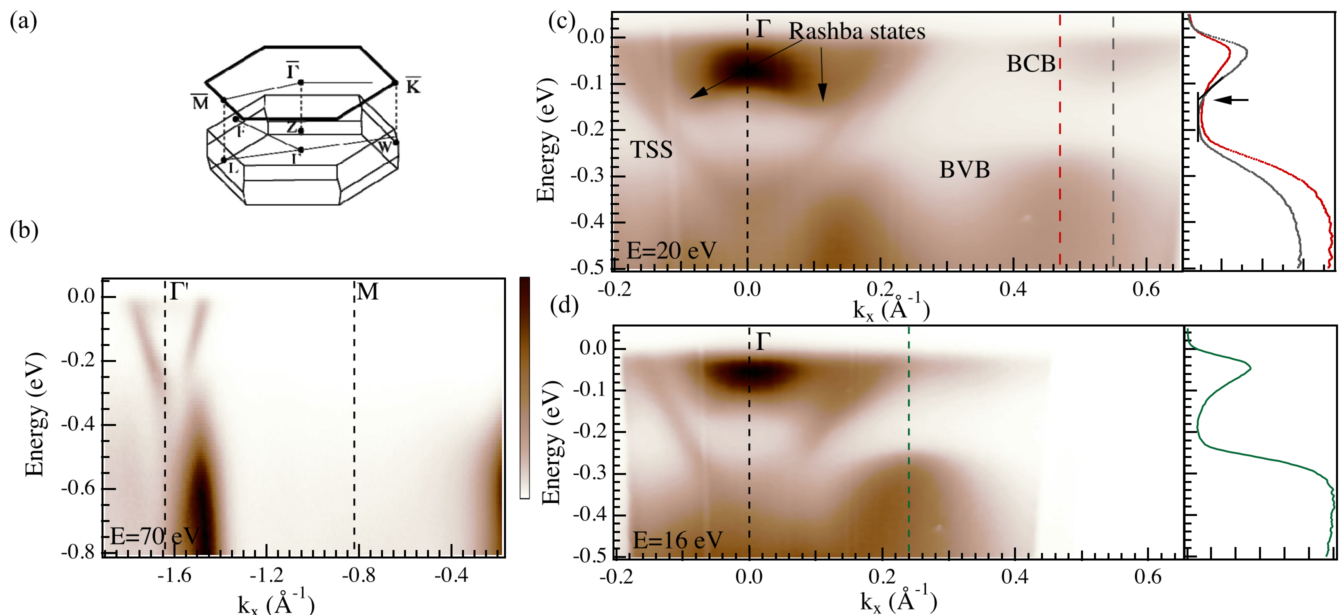

FIG. 2. (a) Sketch of the bulk BZ and SBZ of $SnBi_2Te_4$. (b) Energy-momentum dispersion of $SnBi_2Te_4$ along $\bar{\Gamma}$-$\bar{M}$ of the second SBZ, taken at 70 eV photon energy. (c) Energy-momentum dispersion along $\bar{\Gamma}$-$\bar{M}$ of the first SBZ, taken at 20 eV photon energy. The right panel shows energy distribution curves extracted at $k_x = 0.47$ Å^{-1} (red line) and $k_x = 0.55$ Å^{-1} (gray line). A linear extrapolation of the BCB edge is superimposed. (d) Energy-momentum dispersion along $\bar{\Gamma}$-$\bar{M}$ of the first SBZ, taken at 16 eV photon energy. The right panel shows the energy distribution curve extracted at $k_x = 0.24$ Å^{-1} (green line).

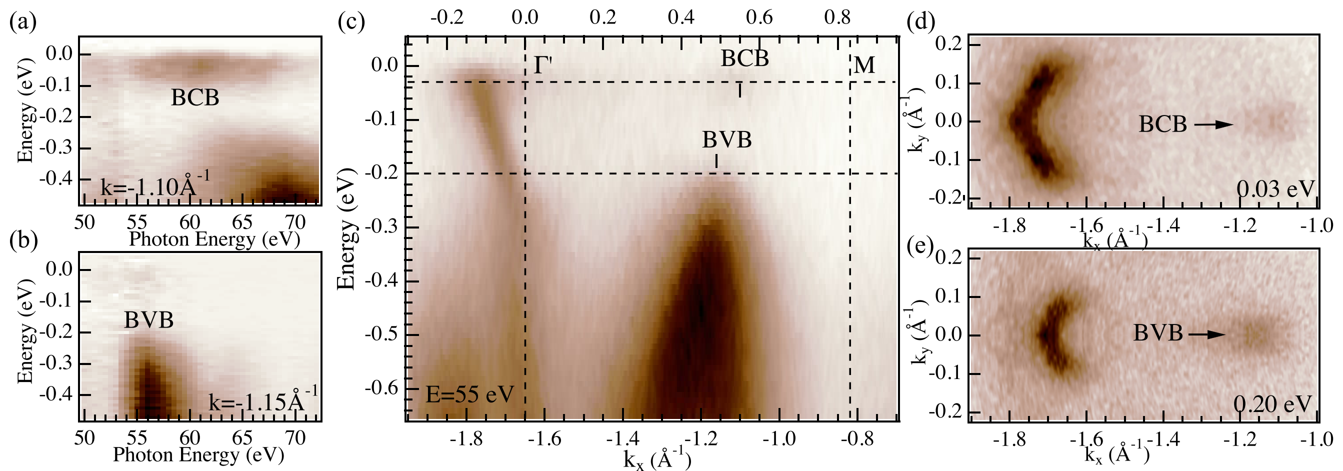

FIG. 3. (a), (b) Photon energy dependence of extracted conduction band minimum at $k_x = -1.10$ Å^{-1}, and valance band maximum at $k_x = -1.15$ Å^{-1}, respectively. (c) Energy-momentum dispersion along $\bar{\Gamma}$-$\bar{M}$ of the second SBZ, taken at 55 eV photon energy. The upper scale is scaled to the first BZ. (d), (e) 2D momentum maps taken at 0.03 eV and 0.20 eV binding energy, respectively. The corresponding binding energies of the maps are indicated in (c) by horizontal dashed lines.

Dirac fermions in $SnBi_2Te_4$ was evaluated to approximately 3.5×10^5 m/s (see Fig. S3 of the Supplemental Material [22]), in line with those in $SnBi_4Te_7$ [49] and in $PbBi_2Te_4$ [17]. The group velocity has been estimated by a linear extrapolation of the data, sufficiently away from the kinks appearing in the vicinity of the bulk bands, where, due to the crystal field, the dispersion usually deviates from the linear behavior and follows the bulk band edge [17]. Going away from the $\bar{\Gamma}$ point along $\bar{\Gamma}$-$\bar{M}$, in Fig. 2(c) we notice two maxima of the BVB centered at $k_x \approx 0.15$ Å^{-1} and $k_x \approx 0.47$ Å^{-1}, and a minimum of the BCB, centered at $k_x \approx 0.55$ Å^{-1}. All of them overlap energetically with the Dirac TSS (see red and gray energy distribution curves referred to the last two peaks). In Fig. 2(d), taken at 16 eV photon energy, we observe a single maximum of the BVB, energetically overlapping with the Dirac TSS (see corresponding green energy distribution curve) and located at $k_x \approx 0.24$ Å^{-1}. Bulk states, other than the M-shaped BVB bands, approaching E_F along $\bar{\Gamma}$-$\bar{M}$ have not been reported for films of $SnBi_2Te_4$ [11], while observed in bulk $PbBi_2Te_4$ [17].

In order to determine the minimum and maximum position of the BCB and BVB we performed photon-energy-dependent measurements [Figs. 3(a) and 3(b)]. From Fig. 3(a) we extract a minimum of the BCB, taken at $k_x = 1.10$ Å^{-1} measured along $\bar{\Gamma}$-$\bar{M}$-$\bar{\Gamma}'$ line (that corresponds to $k_x = 0.55$ Å^{-1} as measured along $\bar{\Gamma}'$-$\bar{M}$), at about 0.13 eV binding energy and 61 eV photon energy, in agreement with the value extracted by linear extrapolation from Fig. 2(c). Slightly closer to the $\bar{\Gamma}'$ point, at $k_x = 1.15$ Å^{-1} (0.50 Å^{-1}), see Fig. 3(b), we find a maximum of the BVB at about 0.18 eV binding energy and 55 eV photon energy. We notice that, due to a small inverse bulk parameter (of ≈0.15 Å^{-1}), the final-state momentum broadening hides the expected dispersion of the occupied initial states [50]. The observed peaks, appearing with little dispersion in Figs. 3(a) and 3(b), are the result of the total DOS averaged along all k_z for the selected $k_\parallel$. In Fig. 3(c), we show ARPES measurements and selected constant energy cuts [Figs. 3(d) and 3(e)] taken at 55 eV photon energy along the $\bar{\Gamma}$-$\bar{M}$-$\bar{\Gamma}'$ direction. These measurements show the BVB close to its edge in energy, and the BCB emerging at E_F while not reaching its maximum depth for this photon energy.

The DFT electronic structure calculations for $SnBi_2Te_4$ were done earlier using the GGA-PBE XC potential [9,38]. These calculations predicted a narrow indirect bulk gap of ≈20 meV, with a maximum of the valence band lying at $k_x =$ 0.25 Å^{-1} along the $\bar{\Gamma}$-$\bar{M}$ in the surface-projected spectrum, and a minimum of the conduction band at $\bar{\Gamma}$.

Here, we first reexamine the bulk spectrum of $SnBi_2Te_4$ by using the modified Becke-Johnson (mBJ) exchange potential [32,33], which has been shown to be the most accurate semilocal potential for calculations of semiconductor band structure. As can be seen in Fig. 4(a), in mBJ spectrum, like in PBE band structure, the minimum of the conduction band lies in the Γ-Z direction while the valence band is characterized by a pronounced tip in the L-Z direction of the BZ of the primitive orthorhombic cell. Note that the valence band maximum is outside the high-symmetry directions of the BZ and it lies at $k_z = -0.3$ $(2\pi/c)$ in the BZ of the hexagonal cell. In particular, the mBJ calculations result in a narrower (by ≈50 meV) gap at the Z point [see Fig. 4(b)], the time-reversal-invariant momentum (TRIM) point where the parity changes sign due to the spin orbit coupling (SOC) induced band inversion [Fig. 4(a)].

In the DFT-1/2 method implementation for normal insulators the cutoff radius $r_{\rm cut}$ in the spherical step function multiplier for the atomic self-energy potential V_S is determined variationally by maximizing the band gap at the Brillouin zone center [34]. In contrast, for band-inverted topological insulators fitting the $r_{\rm cut}$ parameter requires minimizing the gap [51]. In our calculation we have minimized the gap at the Z point where the band inversion occurs. The calculated DFT-1/2 bulk spectrum is in fine agreement with our mBJ calculation results [Figs. 4(a) and 4(b)], especially in the vicinity of the Γ and Z points (which are projected onto the center of the 2D BZ) that makes this method applicable to surface band structure calculations with accuracy of mBJ.

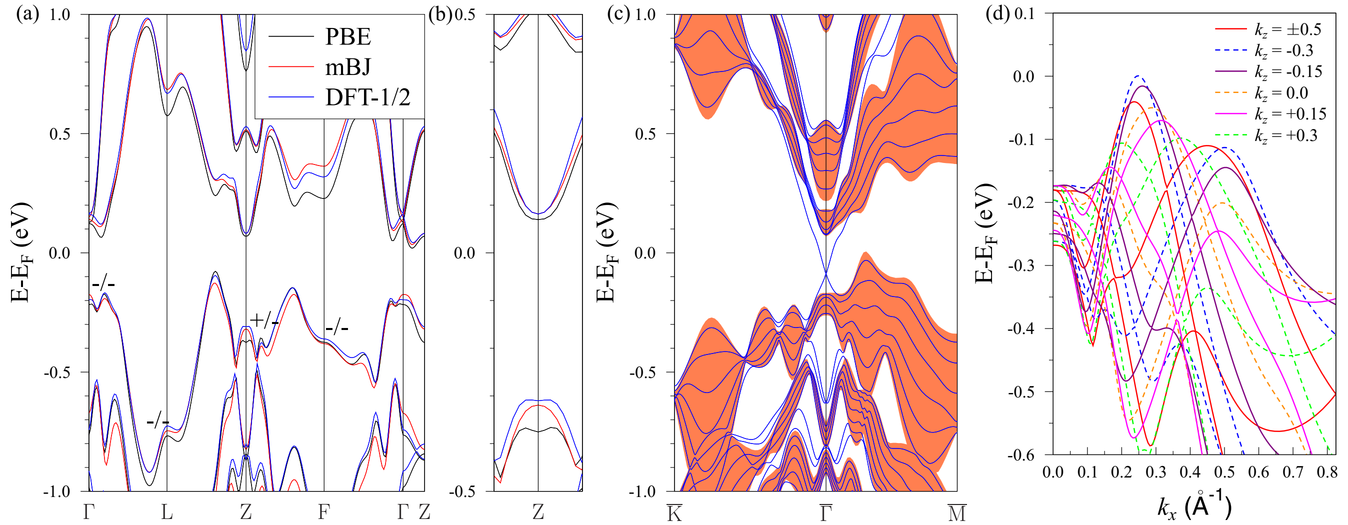

FIG. 4. (a) Bulk band structure of $SnBi_2Te_4$ calculated with different approaches: GGA-PBE, mBJ, and DFT-1/2. Signs of $\delta = \prod_{occ} \xi = \pm1$ (ξ is the parity of occupied bands) at the TRIM are also shown for calculations with/without SOC taken into account. (b) Magnified view of the bulk spectra in the vicinity of the Z point. (c) Surface band structure calculated within DFT-1/2 method. Shaded area marks continuum of the bulk states projected onto (111) surface. (d) Surface-projected upper valence band at the $\bar{\Gamma}$-$\bar{M}$ direction parsed into different k_z contributions.

The surface band structure of $SnBi_2Te_4$ calculated using the DFT-1/2 method is shown in Fig. 4(c). First, the projected bulk spectrum (shaded area) demonstrates the indirect gap of 63 meV that is much larger than the earlier PBE prediction ($\approx$20 meV [9,38]). In turn, the experimental band gap value of $\approx$50 meV calculated within the maximum of the BVB and the minimum of the BCB at $\bar{\Gamma}$ [Figs. 2(c) and 2(d)] and at $k_x = 0.55$ Å^{-1} [Fig. 3(a)] is closer to DFT-1/2 results. However, both PBE and DFT-1/2 methods give the VB maximum position at $k_x = 0.25$ Å^{-1} along $\bar{\Gamma}$-$\bar{M}$. The Dirac point of the topological surface state lies by $\approx$80 meV deeper than the VB maximum. This is in contrast to the PBE result where the Dirac point resides by $\approx$170 meV below the VB maximum [38].

Figure 4(d) shows the surface-projected upper valence band at the $\bar{\Gamma}$-$\bar{M}$ direction parsed into different k_z contributions. As can be seen, for each k_z the upper band has two maxima. In particular, for $-0.5 < k_z < 0$ they are at $k_x \approx 0.25$ and $k_x \approx 0.50$ Å^{-1}. The second maximum can be attributed to the bright BVB feature visible in the ARPES experiments at $k_x \approx 0.50$ Å^{-1} and photon energy of 20 eV and 55 eV, whereas the first one, which contributes to the absolute VB maximum in the calculations, is visible at a photon energy of 16 eV. At the same time, both 0.25 and 0.50 Å^{-1} maxima in ARPES data lie at binding energy of about 200 meV. At first glance, there is not much agreement between calculated and experimental band structure. The reason can be both in the fact that the grown crystal has intermixing on Sn and Bi sublattices and in the fact that ARPES does not fix the top of the valence band at $k_x \approx 0.25$ Å^{-1} where the measured intensity is much lower than that for $k_x \approx 0.50$ Å^{-1}. Since the second maximum in the calculated VB spectrum at $k_x \approx 0.50$ Å^{-1} found at $k_z = -0.4$ [not shown in Fig. 4(d)] lies at -100 meV and taking into account the n doping in the sample of about 100 meV, one can conclude the position of the VB maximum at $k_x \approx 0.50$ Å^{-1} agrees well with ARPES. In addition, the calculations of Fig. 4(c) show a local minimum in the BCB in proximity of $k_x \approx 0.55$ Å^{-1}, in agreement with the experimental results reported in Fig. 3(a).

Next we examine the effect of the Sn-Bi intermixing observed in the grown sample on the $SnBi_2Te_4$ electronic structure. To this end we employ the VCA approximation to describe the presence of Bi atoms on the Sn sublattice and vice versa. As established by our STM measurements the 10%–12% Sn-Bi intermixing takes place in the sample. To simulate this intermixing we constructed $Sn_{0.88}Bi_{0.12}$ and $Bi_{0.94}Sn_{0.06}$ VCA pseudopotentials, which provide an average intermixing ratio of 12% in the $SnBi_2Te_4$ bulk lattice [Fig. 5(a)].

The surface band structure of $SnBi_2Te_4$ with 12% Sn-Bi intermixing is shown in Fig. 5(b). As can be seen, the intermixing results in shifting the topological surface state down to the valence band so that the Dirac point is located at the edge of the bulk continuum, in agreement with the experimental results. Besides, the dispersion of the topological surface state changes from linear, in the vicinity of the Dirac point (for the ideal atomic structure), to nonlinear and differs from the experimental dispersion. Similar dispersion of the Dirac state was observed earlier in TIs with more complicated atomic structure [49,52]. This change in the Dirac state dispersion is mostly related to the structural relaxations within the SL block due to Sn-Bi intermixing that are -0.7%, $+0.9\%$, and -3% for $Sn_{0.88}Bi_{0.12}$-Te, Te-$Bi_{0.94}Sn_{0.06}$, and $Bi_{0.94}Sn_{0.06}$-Te interlayer spacings, respectively, with respect to the corresponding Sn-Te, Te-Bi, and Bi-Te interlayer distances in the ideal crystal structure. If these relaxations are neglected, i.e., in the calculation of $SnBi_2Te_4$ with 12% Sn-Bi intermixing with the ideal atomic structure, the surface spectrum shows almost linear Dirac dispersion [Fig. 5(c)]. Although we cannot compare PBE-based bulk spectrum of the structure with Sn-Bi intermixing quantitatively with the spectrum of the ideal $SnBi_2Te_4$ calculated within the DFT-1/2 approach, the valence band along $\bar{\Gamma}$-$\bar{M}$ in the case of Sn-Bi intermixing also

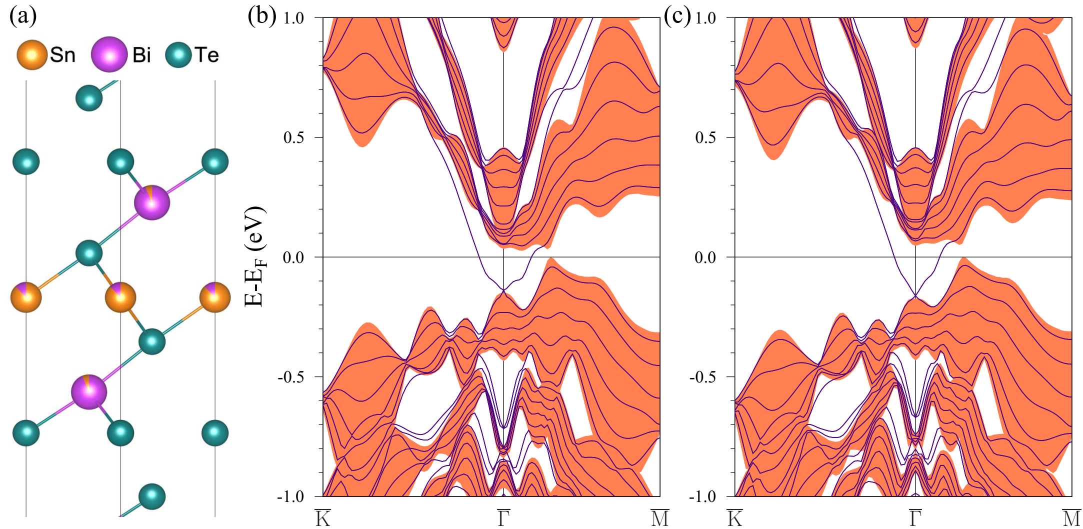

FIG. 5. (a) Atomic structure of $SnBi_2Te_4$ with 12% Sn-Bi intermixing. Surface band structure with (b) and without (c) structural relaxation taken into account.

shows a maximum at $k_x \approx 0.25$ Å^{-1} and the second highest tip (local maximum) at $k_x \approx 0.50$ Å^{-1}, regardless of whether structural relaxation has been taken into account or not.

Overall, the comparison between the theoretical calculations and experimental results leads to a pretty good agreement in k space of relative maxima and minima of BVB and BCB, respectively, that is along $\bar{\Gamma}$-$\bar{M}$ direction of the SBZ, but remains unsatisfactory for the absolute values that give rise to the band gap. Taking into account the Sn-Bi intermixing without structural relaxation [Fig. 5(c)], a shift of the topological surface state within the BVB is well reproduced by the calculations, while leaving a partial agreement on the shape of the projected BVB and BCB.

IV. CONCLUSIONS

In contrast to the direct gap Bi_2Se_3 [53,54], the Bi_2Te_3 [53,55] and related ternary compounds $A^{IV}Bi_2Te_4$ are characterized (according to earlier theoretical calculations [9]) by indirect gap, with a maximum of the BVB lying along the $\bar{\Gamma}$-$\bar{M}$ direction of the SBZ (at ≈1/4–1/3 $\bar{\Gamma}$-$\bar{M}$) and second highest maximum at larger $k_\parallel$. However, not much is reported in the literature about a precise experimental investigation of the bulk electronic structure for this class of TIs far from the SBZ center [15,17]. In the $PbBi_2Te_4$ [17] compound the BVB maximum was found, with photon energy of $h\nu = 10$ eV, at large $k_\parallel \approx 0.4$ Å^{-1}. According to earlier PBE-based calculations [9,38], $SnBi_2Te_4$ having small indirect gap is characterized by the $\bar{\Gamma}$ Dirac state in the surface spectrum heavily overlapping with BVB states. In the present work we revised the DFT band structure applying advanced exchange-correlation functionals and accounted the presence of Sn-Bi intermixing in the grown crystals, the degree of which was found by means of STM measurements to be quite significant, of 10%–12%. As well we have performed comprehensive ARPES measurements within a wide range of the photon energies. Despite the alterations of the bulk and surface spectra due to different XC functionals and Sn-Bi intermixing, the main features of the theoretical spectra remain unchanged demonstrating a Dirac state overlapping with $\bar{\Gamma}$-$\bar{M}$ BVB states which possess two maxima, absolute and the second highest at relatively small ($k_x \approx 0.25$ Å^{-1}) and large ($k_x \approx 0.50$ Å^{-1}) $k_\parallel$ vectors, respectively, although accounting of the Sn-Bi intermixing leads to a better matching with the experimental results.

ARPES results on $SnBi_2Te_4$ crystals revealed a considerable energy overlap of the Dirac state with the BVB and BCB along the $\bar{\Gamma}$-$\bar{M}$ direction. This overlap places limits in the use of the spin-polarized Dirac state of this compound, unless the Fermi level is further moved into the indirect bulk band gap. This step forward may be achieved, for instance, by chemical doping of the $SnBi_2Te_4$ stoichiometry. The band gap was experimentally found to be ≈50 meV, with the minimum of the BCB at $\bar{\Gamma}$ and at $k_x \approx 0.55$ Å^{-1}, and the maximum of the BVB at $k_x \approx 0.50$ Å^{-1}, both along the $\bar{\Gamma}$-$\bar{M}$ direction. The provided characterization of the band structure may explain the origin of the residual three-dimensional bulk contribution across E_F reflected in magnetotransport measurements of the $SnBi_2Te_4$ compound [12].

ACKNOWLEDGMENTS

We acknowledge Elettra Sincrotrone Trieste for providing access to its synchrotron radiation facilities and for financial support. This research was supported in part by the Progetto STAR 2 (PIR01-00008) of the Italian Ministry of Education, University, and Research. We acknowledge EUROFEL-ROADMAP ESFRI of the Italian Ministry of Education, University, and Research. The density functional theory calculations were supported by the government research assignment for ISPMS SB RAS, Project No. FWRW-2022-0001. E.V.C. acknowledges support from Saint Petersburg State University (Project ID No. 94031444). The calculations were partially performed using the equipment of the Shared Resource Center “Far Eastern Computing Resource” of IACP FEB RAS [56].

[1] K. Kondou, R. Yoshimi, A. Tsukazaki, Y. Fukuma, J. Matsuno, K. S. Takahashi, M. Kawasaki, Y. Tokura, and Y. Otani, Nat. Phys. **12**, 1027 (2016).

[2] J. Han, A. Richardella, S. A. Siddiqui, J. Finley, N. Samarth, and L. Liu, Phys. Rev. Lett. **119**, 077702 (2017).

[3] R. Sun, S. Yang, X. Yang, E. Vetter, D. Sun, N. Li, L. Su, Y. Li, Y. Li, Z.-Z. Gong, Z.-K. Xie, K.-Y. Hou, Q. Gul, W. He, X.-Q. Zhang, and Z.-H. Cheng, Nano Lett. **19**, 4420 (2019).

[4] Y. Wang, R. Ramaswamy, and H. Yang, J. Phys. D **51**, 273002 (2018).

[5] Y. Shiomi, K. Nomura, Y. Kajiwara, K. Eto, M. Novak, K. Segawa, Y. Ando, and E. Saitoh, Phys. Rev. Lett. **113**, 196601 (2014).

[6] J.-C. Rojas-Sánchez, S. Oyarzún, Y. Fu, A. Marty, C. Vergnaud, S. Gambarelli, L. Vila, M. Jamet, Y. Ohtsubo, A. Taleb-Ibrahimi, P. Le Fèvre, F. Bertran, N. Reyren, J.-M. George, and A. Fert, Phys. Rev. Lett. **116**, 096602 (2016).

[7] Y. L. Chen, J. G. Analytis, J.-H. Chu, Z. K. Liu, S.-K. Mo, X. L. Qi, H. J. Zhang, D. H. Lu, X. Dai, Z. Fang, S. C. Zhang, I. R. Fisher, Z. Hussain, and Z.-X. Shen, Science **325**, 178 (2009).

[8] C.-Z. Chang, P. Tang, Y.-L. Wang, X. Feng, K. Li, Z. Zhang, Y. Wang, L.-L. Wang, X. Chen, C. Liu, W. Duan, K. He, X.-C. Ma, and Q.-K. Xue, Phys. Rev. Lett. **112**, 056801 (2014).

[9] S. V. Eremeev, G. Landolt, T. V. Menshchikova, B. Slomski, Y. M. Koroteev, Z. S. Aliev, M. B. Babanly, J. Henk, A. Ernst, L. Patthey, A. Eich, A. A. Khajetoorians, J. Hagemeister, O. Pietzsch, J. Wiebe, R. Wiesendanger, P. M. Echenique, S. S. Tsirkin, I. R. Amiraslanov, J. H. Dil, and E. V. Chulkov, Nat. Commun. **3**, 635 (2012).

[10] E. Rongione, S. Fragkos, L. Baringthon, J. Hawecker, E. Xenogiannopoulou, P. Tsipas, C. Song, M. Mičica, J. Mangeney, J. Tignon, T. Boulier, N. Reyren, R. Lebrun, J.-M. George, P. Le Fèvre, S. Dhillon, A. Dimoulas, and H. Jaffrès, Adv. Opt. Mater. **10**, 2102061 (2022).

[11] S. Fragkos, L. Baringthon, P. Tsipas, E. Xenogiannopoulou, P. Le Fèvre, P. Kumar, H. Okuno, N. Reyren, A. Lemaitre, G. Patriarche, J.-M. George, and A. Dimoulas, Phys. Rev. Mater. **5**, 014203 (2021).

[12] Y.-C. Zou, Z.-G. Chen, E. Zhang, F. Kong, Y. Lu, L. Wang, J. Drennan, Z. Wang, F. Xiu, K. Cho, and J. Zou, Nano Res. **11**, 696 (2018).

[13] M. Neupane, S.-Y. Xu, L. A. Wray, A. Petersen, R. Shankar, N. Alidoust, C. Liu, A. Fedorov, H. Ji, J. M. Allred, Y. S. Hor, T.-R. Chang, H.-T. Jeng, H. Lin, A. Bansil, R. J. Cava, and M. Z. Hasan, Phys. Rev. B **85**, 235406 (2012).

[14] I. A. Shvets, I. I. Klimovskikh, Z. S. Aliev, M. B. Babanly, J. Sánchez-Barriga, M. Krivenkov, A. M. Shikin, and E. V. Chulkov, Phys. Rev. B **96**, 235124 (2017).

[15] S. Souma, K. Eto, M. Nomura, K. Nakayama, T. Sato, T. Takahashi, K. Segawa, and Y. Ando, Phys. Rev. Lett. **108**, 116801 (2012).

[16] K. Kuroda, M. Ye, A. Kimura, S. V. Eremeev, E. E. Krasovskii, E. V. Chulkov, Y. Ueda, K. Miyamoto, T. Okuda, K. Shimada, H. Namatame, and M. Taniguchi, Phys. Rev. Lett. **105**, 146801 (2010).

[17] K. Kuroda, H. Miyahara, M. Ye, S. V. Eremeev, Y. M. Koroteev, E. E. Krasovskii, E. V. Chulkov, S. Hiramoto, C. Moriyoshi, Y. Kuroiwa, K. Miyamoto, T. Okuda, M. Arita, K. Shimada, H. Namatame, M. Taniguchi, Y. Ueda, and A. Kimura, Phys. Rev. Lett. **108**, 206803 (2012).

[18] M. M. Otrokov, I. I. Klimovskikh, H. Bentmann, D. Estyunin, A. Zeugner, Z. S. Aliev, S. Gaß, A. U. B. Wolter, A. V. Koroleva, A. M. Shikin, M. Blanco-Rey, M. Hoffmann, I. P. Rusinov, A. Y. Vyazovskaya, S. V. Eremeev, Y. M. Koroteev, V. M. Kuznetsov, F. Freyse, J. Sánchez-Barriga, I. R. Amiraslanov, M. B. Babanly, N. T. Mamedov, N. A. Abdullayev, V. N. Zverev, A. Alfonsov, V. Kataev, B. Büchner, E. F. Schwier, S. Kumar, A. Kimura, L. Petaccia, G. Di Santo, R. C. Vidal, S. Schatz, K. Kißner, M. Ünzelmann, C. H. Min, S. Moser, T. R. F. Peixoto, F. Reinert, A. Ernst, P. M. Echenique, A. Isaeva, and E. V. Chulkov, Nature (London) **576**, 416 (2019).

[19] I. Lee, C. K. Kim, J. Lee, S. J. L. Billinge, R. Zhong, J. A. Schneeloch, T. Liu, T. Valla, J. M. Tranquada, G. Gu, and J. C. S. Davis, Proc. Natl. Acad. Sci. USA **112**, 1316 (2015).

[20] M. Garnica, M. M. Otrokov, P. C. Aguilar, I. I. Klimovskikh, D. Estyunin, Z. S. Aliev, I. R. Amiraslanov, N. A. Abdullayev, V. N. Zverev, M. B. Babanly, N. T. Mamedov, A. M. Shikin, A. Arnau, A. L. V. de Parga, E. V. Chulkov, and R. Miranda, npj Quantum Mater. **7**, 7 (2022).

[21] D. Niesner, S. Otto, V. Hermann, T. Fauster, T. V. Menshchikova, S. V. Eremeev, Z. S. Aliev, I. R. Amiraslanov, M. B. Babanly, P. M. Echenique, and E. V. Chulkov, Phys. Rev. B **89**, 081404(R) (2014).

[22] See Supplemental Material at http://link.aps.org/supplemental/10.1103/PhysRevMaterials.7.014203 for diffraction pattern and structural data of $SnBi_2Te_4$, core level measurements and a low energy electron diffraction pattern, and a linear fit of the topological surface state.

[23] L. Petaccia, P. Vilmercati, S. Gorovikov, M. Barnaba, A. Bianco, D. Cocco, C. Masciovecchio, and A. Goldoni, Nucl. Instrum. Methods Phys. Res. Sect. A **606**, 780 (2009).

[24] I. Horcas, R. Fernández, J. M. Gómez-Rodríguez, J. Colchero, J. Gómez-Herrero, and A. M. Baro, Rev. Sci. Instrum. **78**, 013705 (2007).

[25] P. E. Blöchl, Phys. Rev. B **50**, 17953 (1994).

[26] G. Kresse and J. Hafner, Phys. Rev. B **47**, 558 (1993).

[27] G. Kresse and J. Furthmüller, Phys. Rev. B **54**, 11169 (1996).

[28] G. Kresse and J. Furthmüller, Comput. Mater. Sci. **6**, 15 (1996).

[29] J. P. Perdew, K. Burke, and M. Ernzerhof, Phys. Rev. Lett. **77**, 3865 (1996).

[30] D. Koelling and B. Harmon, J. Phys. C **10**, 3107 (1977).

[31] S. Grimme, J. Antony, S. Ehrlich, and H. Krieg, J. Chem. Phys. **132**, 154104 (2010).

[32] A. D. Becke and E. R. Johnson, J. Chem. Phys. **124**, 221101 (2006).

[33] F. Tran and P. Blaha, Phys. Rev. Lett. **102**, 226401 (2009).

[34] L. G. Ferreira, M. Marques, and L. K. Teles, Phys. Rev. B **78**, 125116 (2008).

[35] L. G. Ferreira, M. Marques, and L. K. Teles, AIP Adv. **1**, 032119 (2011).

[36] X. Gonze, B. Amadon, P.-M. Anglade, J.-M. Beuken, F. Bottin, P. Boulanger, F. Bruneval, D. Caliste, R. Caracas, M. Côté, T. Deutsch, L. Genovese, P. Ghosez, M. Giantomassi, S. Goedecker, D. R. Hamann, P. Hermet, F. Jollet, G. Jomard, S. Leroux, M. Mancini, S. Mazevet, M. J. T. Oliveira, G. Onida, Y.

Pouillon, T. Rangel, G.-M. Rignanese, D. Sangalli, R. Shaltaf, M. Torrent, M. J. Verstraete, G. Zerah, and J. W. Zwanziger, Comput. Phys. Commun. **180**, 2582 (2009).

[37] M. Krack, Theor. Chem. Acc. **114**, 145 (2005).

[38] M. G. Vergniory, T. V. Menshchikova, I. V. Silkin, Y. M. Koroteev, S. V. Eremeev, and E. V. Chulkov, Phys. Rev. B **92**, 045134 (2015).

[39] Y. Yuan, X. Wang, H. Li, J. Li, Y. Ji, Z. Hao, Y. Wu, K. He, Y. Wang, Y. Xu, W. Duan, W. Li, and Q.-K. Xue, Nano Lett. **20**, 3271 (2020).

[40] M. Nomura, S. Souma, A. Takayama, T. Sato, T. Takahashi, K. Eto, K. Segawa, and Y. Ando, Phys. Rev. B **89**, 045134 (2014).

[41] D. Pacilè, S. V. Eremeev, M. Caputo, M. Pisarra, O. De Luca, I. Grimaldi, J. Fujii, Z. S. Aliev, M. B. Babanly, I. Vobornik, R. G. Agostino, A. Goldoni, E. V. Chulkov, and M. Papagno, Phys. Status Solidi RRL **12**, 1800341 (2018).

[42] M. Papagno, S. V. Eremeev, J. Fujii, Z. S. Aliev, M. B. Babanly, S. K. Mahatha, I. Vobornik, N. T. Mamedov, D. Pacilè, and E. V. Chulkov, ACS Nano **10**, 3518 (2016).

[43] M. Bianchi, R. C. Hatch, Z. Li, P. Hofmann, F. Song, J. Mi, B. B. Iversen, Z. M. Abd El-Fattah, P. Löptien, L. Zhou, A. A. Khajetoorians, J. Wiebe, R. Wiesendanger, and J. W. Wells, ACS Nano **6**, 7009 (2012).

[44] Z.-H. Zhu, G. Levy, B. Ludbrook, C. N. Veenstra, J. A. Rosen, R. Comin, D. Wong, P. Dosanjh, A. Ubaldini, P. Syers, N. P. Butch, J. Paglione, I. S. Elfimov, and A. Damascelli, Phys. Rev. Lett. **107**, 186405 (2011).

[45] H. M. Benia, C. Lin, K. Kern, and C. R. Ast, Phys. Rev. Lett. **107**, 177602 (2011).

[46] S. V. Eremeev, M. G. Vergniory, T. V. Menshchikova, A. A. Shaposhnikov, and E. V. Chulkov, New J. Phys. **14**, 113030 (2012).

[47] L. Plucinski, A. Herdt, S. Fahrendorf, G. Bihlmayer, G. Mussler, S. Döring, J. Kampmeier, F. Matthes, D. E. Bürgler, D. Grützmacher, S. Blügel, and C. M. Schneider, J. Appl. Phys. **113**, 053706 (2013).

[48] E. Frantzeskakis, S. V. Ramankutty, N. de Jong, Y. K. Huang, Y. Pan, A. Tytarenko, M. Radovic, N. C. Plumb, M. Shi, A. Varykhalov, A. de Visser, E. van Heumen, and M. S. Golden, Phys. Rev. X **7**, 041041 (2017).

[49] I. Grimaldi, D. Pacilè, S. V. Eremeev, O. De Luca, A. Policicchio, P. Moras, P. M. Sheverdyaeva, A. K. Kundu, Z. S. Aliev, P. Rudolf, R. G. Agostino, E. V. Chulkov, and M. Papagno, Phys. Rev. B **102**, 085118 (2020).

[50] V. N. Strocov, J. Electron Spectrosc. Relat. Phenom. **130**, 65 (2003).

[51] T. Mota, F. Matusalem, M. Marques, L. K. Teles, and I. Guilhon, J. Phys.: Condens. Matter **34**, 465501 (2022).

[52] S. V. Eremeev, T. V. Menshchikova, I. V. Silkin, M. G. Vergniory, P. M. Echenique, and E. V. Chulkov, Phys. Rev. B **91**, 245145 (2015).

[53] O. V. Yazyev, E. Kioupakis, J. E. Moore, and S. G. Louie, Phys. Rev. B **85**, 161101(R) (2012).

[54] I. A. Nechaev, R. C. Hatch, M. Bianchi, D. Guan, C. Friedrich, I. Aguilera, J. L. Mi, B. B. Iversen, S. Blügel, P. Hofmann, and E. V. Chulkov, Phys. Rev. B **87**, 121111(R) (2013).

[55] I. A. Nechaev and E. V. Chulkov, Phys. Rev. B **88**, 165135 (2013).

[56] See https://cc.dvo.ru.